

Trevor M. Cory
Department of Mechanical Engineering,
The Pennsylvania State University,
University Park, PA 16801
e-mail: tmc5478@psu.edu

Ryan D. Edelson
Department of Mechanical Engineering,
The Pennsylvania State University,
University Park, PA 16801
e-mail: rde5073@psu.edu

Karen A. Thole
Department of Mechanical Engineering,
The Pennsylvania State University,
University Park, PA 16801
e-mail: kthole@psu.edu

Tyler Vincent
Pratt & Whitney, A Division of Raytheon
Technologies Corporation,
East Hartford, CT 06118
e-mail: tyler.vincent2@prattwhitney.com

San Quach
Pratt & Whitney, A Division of Raytheon
Technologies Corporation,
East Hartford, CT 06118
e-mail: san.quach@prattwhitney.com

Dominic Mongillo
Pratt & Whitney, A Division of Raytheon
Technologies Corporation,
East Hartford, CT 06118
e-mail: dominic.mongillo@prattwhitney.com

Impact of Ceramic Matrix Composite Topology on Friction Factor and Heat Transfer

Ceramic matrix composites (CMCs) are of interest for hot section components of gas turbine engines due to their low weight and favorable thermal properties. To implement this advanced composite in a gas turbine engine, characterizing the influence of CMC's surface topology on heat transfer and cooling performance is critical. However, very few published studies have reported the flow and heat transfer effects caused by this unique surface topology. This study is an experimental and computational investigation to evaluate the effect of weave orientations, relevant to CMC surfaces, on the resulting pressure loss and convective heat transfer within an internal channel. The weave pattern was additively manufactured as the walls of a scaled-up coupon containing a single channel. For each of the three weave orientations, bulk pressure losses and convective heat transfer coefficients were measured over a range of Reynolds numbers. Scaling the pressure losses in terms of a friction factor and convective heat transfer coefficients in terms of a Nusselt number showed the importance of choosing the appropriate definition of the hydraulic diameter, which was particularly important for the friction factor. A coupon having one wall with the weave surface increased pressure loss and heat transfer compared to a smooth wall with the largest increases occurring when the CMC weave strands were perpendicular to the flow. Friction factor augmentations were much higher than heat transfer augmentations. When adding the weave to a second channel wall, pressure loss and heat transfer were further increased. Orienting the CMC strands perpendicular to the flow consistently showed the largest augmentations in heat transfer over a smooth channel, but at a much higher pressure loss penalty than that seen with the CMC strands parallel to the flow. [DOI: 10.1115/1.4052355]

Keywords: fluid dynamics and heat transfer phenomena in compressor and turbine components of gas turbine engines, heat transfer and film cooling

Introduction

Ceramic matrix composites (CMC) have the potential to improve the efficiency of a gas turbine engine through enabling high firing temperatures while reducing the amount of coolant air required. CMCs are made up of ceramic fibers embedded in a ceramic matrix, helping to reduce the brittle nature of ceramics while maintaining ceramic's advantageous thermal properties. Low weight and high-temperature capabilities give CMCs significant advantages over the incumbent nickel super alloys commonly used in today's gas turbines [1,2]. The use of CMC components within gas turbines has been found to reduce the weight, and therefore, increase the thrust-to-weight ratio [3] as well as enable high power density and more efficient engines [4]. A parametric study by Tong [5] found that using CMC stator vanes in a two-stage high-pressure turbine reduces thrust-specific fuel consumption by up to 1.5%. Additionally, a CMC combustor liner was found to reduce the landing-and-takeoff NO_x emissions by over 40% due to lowering the required liner cooling [5].

With the ability to withstand high temperatures, the full impact of CMCs, including the resulting surface topology, needs to be understood. One of many differences between CMCs and traditional cast turbine components is the inherent roughness created by the CMC's weave. This unique topology creates macro-roughness features that influence the aerodynamic and heat transfer performance. When

delving deeper into the subject of this pattern topology, various weave orientations can induce different effects on cooling performance. The research in this study is unique because of the specific weave effects chosen as well as the approach to evaluate the effects on channel heat transfer and pressure loss.

Literature Review

As previously stated, CMCs have significant advantages over materials used in present gas turbine engines. Namely, the low weight and ability of CMCs to withstand high temperatures [1,2] can allow their use to enable more efficient engines [4,5]. Many studies have investigated the development of the mechanical properties of CMCs and their abilities to withstand harsh and high-temperature environments. Zhu et al. [6] provide an overview of the development of CMCs, describing how the further progress of CMCs will result in a steep increase in gas turbine temperature capabilities. Zhu et al. [6] also detail mechanical properties such as tensile strength, elastic modulus, and rupture strength associated with a few different CMC fiber types. The oxidation and morphology of environmental barrier coated and uncoated CMCs when exposed to high temperatures have been investigated by Alvin et al. [7]. Multiple studies have reported on the effects of high temperatures and thermal stresses on CMCs [6,8,9]. Furthermore, Watanabe et al. [10,11] conducted studies demonstrating the capabilities of CMC vanes and blades in various cyclic loading and spin tests.

Despite the growing amount of research concerning the structural properties of CMCs, few published studies have focused on how the surface topology of a CMC weave can affect convective heat

Contributed by the International Gas Turbine Institute (IGTI) of ASME for publication in the JOURNAL OF TURBOMACHINERY. Manuscript received July 15, 2021; final manuscript received August 31, 2021; published online October 1, 2021. Tech. Editor: David G. Bogard.

transfer performance. Unlike cast or machined surfaces, CMCs have a unique surface roughness in the form of woven ceramic fibers that have an effect on convective heat transfer. When studying the interaction between an impinging jet and an additively manufactured (AM) CMC weave pattern, Krishna et al. [12] observed an augmentation of Nusselt number for a weaved surface relative to that of a smooth surface. In their preliminary study, their results indicated a strong dependence of the heat transfer on the orientation of the CMC weave pattern relative to the impinging jet. In a later study, Krishna et al. [13] attributed the dominant effect on the heat transfer augmentation from their previous study [12] to additive manufacturing roughness rather than the actual CMC weave pattern. Using a machined surface to better match the weave pattern, heat transfer augmentation was determined to be within experimental uncertainty.

Wilkins et al. [14] investigated the effects of a CMC weave pattern on local heat transfer augmentation and boundary layer development for an external flow using a scaled-up, additively manufactured 5-harness satin (5HS) weave pattern. When the weave pattern was rotated such that the longer CMC strands were perpendicular to the flow, larger local variations in Stanton number results were observed compared to other weave orientations. However, area-averaged results showed little increase in overall heat transfer.

The majority of public CMC research has been reported on the development of this advanced material's structural properties. Using the 5-harness satin weave pattern provided by Nemeth et al. [15] and also used by Wilkins et al. [14], the current study is a unique investigation on the effects of a representative CMC weave on internal convective heat transfer and pressure drop. Our

study aims to fill an important gap in considering the usage of CMCs for turbine applications.

Weave Pattern Geometry and Manufacturing

Single-channel coupons with weave patterns on either one wall (1W) or two walls (2W) that were representative of a CMC surface were additively manufactured. To isolate the effects of the weave pattern and avoid those caused by AM roughness, the weave pattern in this study was scaled up from traditional CMC fiber sizes by a factor of 3.8. Figure 1 shows the description of the coupons, starting with the coupon dimensions in Fig. 1(a). To minimize entrance effects, the L/D_h of each coupon was approximately 18. The weave surfaces of the internal channel walls were created by overlaying six adjacent repeating unit cells (RUCs) containing the weave. Depending upon the particular coupon, the weave was placed either on one wall or two walls of the channel marked by W, as shown by Fig. 1(b). The weave pattern investigated in this study was a 5HS weave described by Nemeth et al. [15], which is a repeatable weave pattern representative of CMCs. This was created in TEXGEN [16], a program that generates user-defined weave patterns. The 5HS square weave RUC is shown in Figs. 1(c) and 1(d). Within the 5HS pattern, each of the five long tows is overlapped by one of the five cross tows once per RUC. Relative to the 5HS pattern in Nemeth et al. [15], the weave in this study was created with a slightly thicker fabric to produce more definition between the intersecting tows. Dimensions for the RUC are listed in Table 1 in terms of the average channel height (H) and width (W). The root mean square (RMS) roughness of the weave pattern was determined by fitting the design intent RUC to the AM RUC. The height differences between the AM weave surface and design intent were used to calculate the RMS roughness as shown by Eq. (1), where M is the number of data points along the weave surface. The RMS roughness of the weave was 0.04H.

All coupons were AM in halves with a state-of-the-art direct metal laser sintering machine. Each coupon half consisted of the entire coupon length and one of the large internal walls, as shown by Fig. 1(b). The halves were printed with the weave pattern facing upward so that AM printing effects would be minimized. All coupons were printed from Inconel 718, except for the 90-1W coupon, which was made of Hastelloy X. All coupon halves were removed from the build plate and cut to the proper dimensions by wire electrical discharge machining. Finally, each coupon half was welded to its counterpart along section A-A seen in Fig. 1(a) to finish the manufacturing process.

$$RMS_w = \sqrt{\frac{1}{M} \sum_{i=1}^M (z_{surf} - z_{des})_i^2} \quad (1)$$

A total of seven coupons were printed as shown in Table 2, where the naming convention consists of the weave angle (0 deg, 45 deg, and 90 deg) as well as whether the weave was on one or two-channel walls. Three different weave orientation angles and two different weave alignments were chosen in this study. The weave orientations are shown in Fig. 2. In the 0 deg orientation, the long weave tows that cover most of the surface were parallel to the

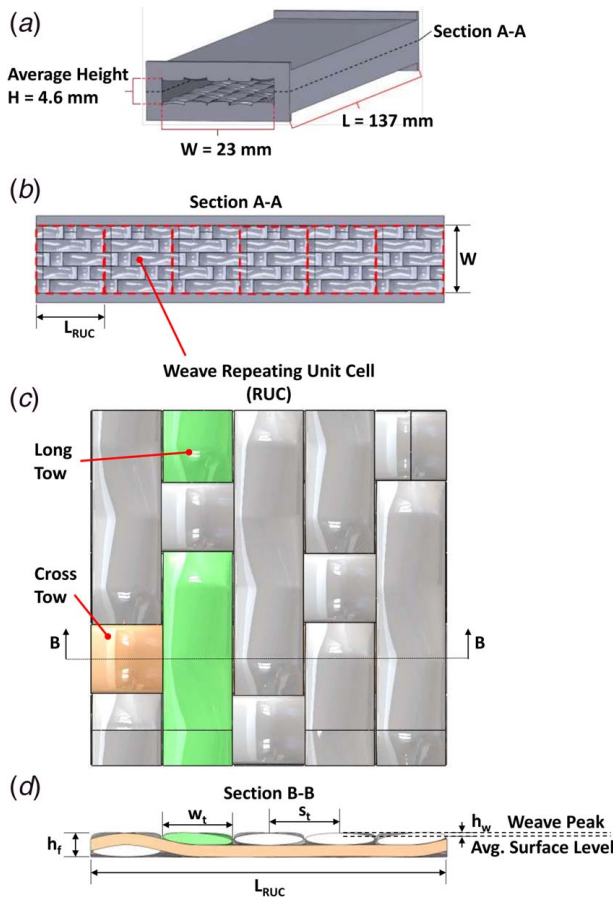


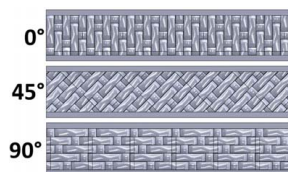
Fig. 1 (a) shows the coupon model with design channel dimensions and (b) shows a cross section view of the bottom channel wall with a weave surface created by six adjacent weave RUCs. (c, d) show a top-down view and side cross section view of the RUC.

Table 1 RUC dimensions

Parameter	Size
RUC length, L_{RUC}	1.0W
Tow width, w_t	0.19W
Tow pitch, s_t	0.20W
Fabric height, h_f	0.32H
Weave peak, h_w	0.04H

Table 2 Coupon geometry types

Coupon name	Weave orientation (deg)	Weave walls	Aspect ratio
0-1W	0	1 Wall	5
45-1W	45	1 Wall	5
90-1W	90	1 Wall	5
0-2W-A	0	2 Aligned walls	5
0-2W-S	0	2 Staggered walls	5
90-2W-A	90	2 Aligned walls	5
90-2W-S	90	2 Staggered walls	5

**Fig. 2 Top-down view of the bottom channel walls for the three different weave orientation angles**

direction of channel flow. In the 90 deg orientation, the long tows were perpendicular to the flow. All channel aspect ratios (AR) were 5:1.

Also evaluated in this study was the weave alignment for the 0 deg and 90 deg orientations by placing the weave patterns on both the top and bottom channel walls. The channel sidewalls were smooth. In the aligned cases, the top and bottom wall weave patterns were identical. In the staggered cases, the top wall weave was offset from the bottom by $L_{RUC}/2$, as shown in Fig. 3.

Upon completion of the manufacturing, the as-built channel dimensions were calculated by taking computed tomography (CT) scans of each test coupon. Specialized software was used to calculate channel perimeter, cross-sectional area, surface area, and wall thickness. However, with complex weave surface topology, calculating these parameters can be done in a number of different ways. As such, two calculation methods were implemented in this study. The first method, referred to as Method 1, consisted of calculating the hydraulic diameter (D_h) at various cross-sectional slices down the length of the channel as shown by Eq. (2) and Fig. 4(a), where N equals the number of slices. The cross-sectional area of each slice was calculated by determining the size and number of CT pixels within the open channel area of the slice image. The perimeter of each slice was calculated by the number of pixels along the edge of the open channel area.

$$D_h = \frac{1}{N} \sum_{i=1}^N 4 \frac{A_{c,i}}{P_i} \quad (2)$$

Method 2 for calculating D_h was based on placing a rectangular channel in which the rectangle's bounds lined up with the average minimum to maximum height of the channel's walls as shown by

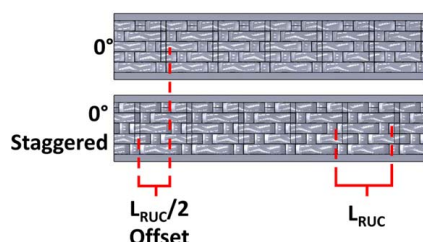
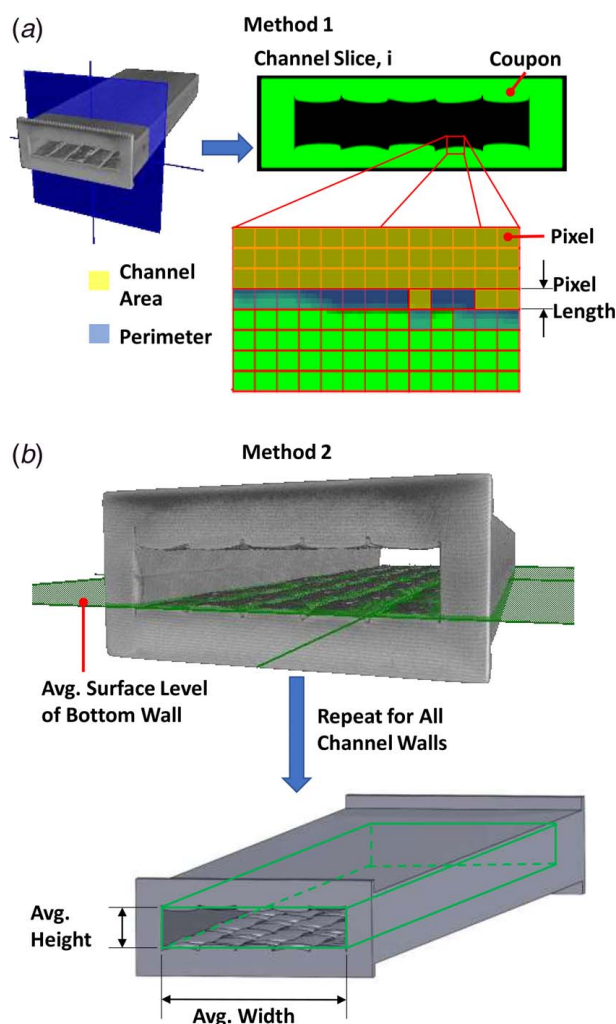
**Fig. 3 Top-down view of the 0 deg weave channel walls for the aligned case (top) and for the staggered weave pattern**

Fig. 4(b). The average surface height of each internal channel wall was determined using the CT scan data.

The main point of interest within the two-parameter calculation methods was the substantial difference in D_h . This disparity is seen in Fig. 5, where the D_h calculated using Method 2 is consistently larger than that of Method 1 for each of the coupons tested. The percent difference between D_h calculation methods across each coupon ranges from 7% in the 90-2W-S coupon and up to 20% in the 0-2W-A coupon. The presence of the weave pattern surface adds additional surface area due to the valleys of the weave surface. This relative change causes Method 1, which calculates D_h at numerous cross-sections and takes an average value for the channel, to yield a smaller D_h compared to Method 2. The differences in the D_h of each method have a large impact on the friction factor results as discussed in the Results section of this paper.

Experimental Setup and Methodology

Pressure losses and convective heat transfer experiments were conducted using a test rig similar to those used by Stimpson et al. [17] and Snyder et al. [18]. Figure 6 depicts a cross-sectional view of the test rig consisting of two plenums located upstream and downstream of the test coupon. The upstream plenum supplies the inlet of the coupon with a uniform velocity flow. The downstream plenum provides a rapid expansion of the flow as it exits the channel.

**Fig. 4 Different methods for calculating D_h using (a) Method 1 with cross-sectional slices of the channel and (b) Method 2 with a fixed rectangular shape**

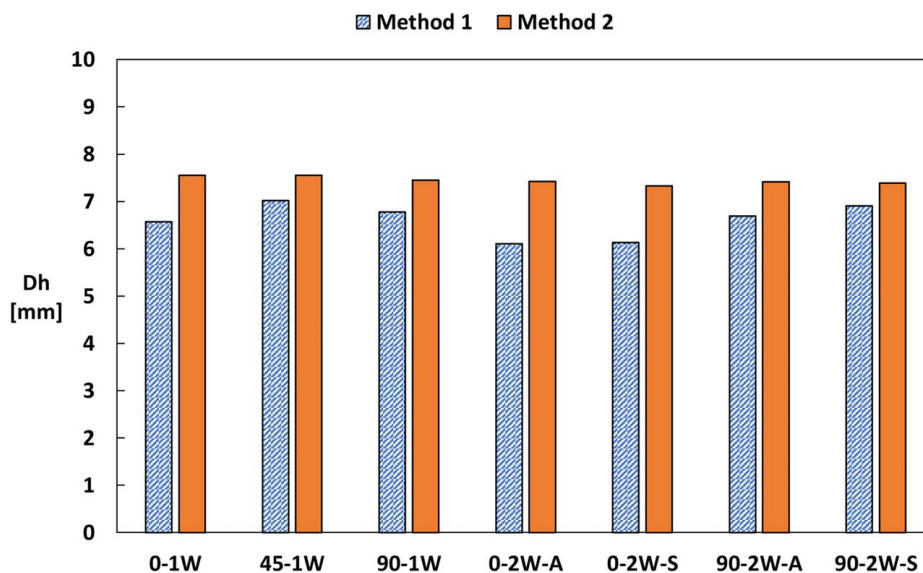


Fig. 5 D_h of each coupon geometry using calculation methods 1 and 2

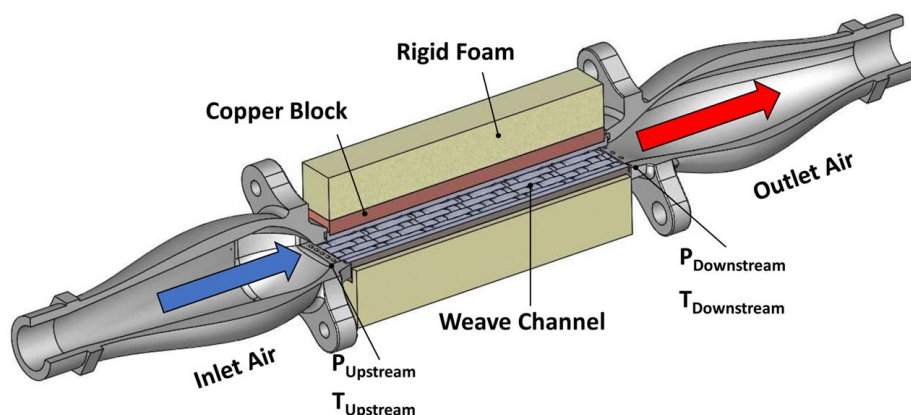


Fig. 6 Schematic of experimental rig used for pressure drop and heat transfer experiments

The pressure loss for each coupon was measured using static pressure taps placed upstream of the coupon inlet and downstream of the exit to measure the pressure change across the coupon. Inlet and exit losses of the plenums were calculated and accounted for to obtain an accurate pressure decrease across the coupon alone. A smooth coupon with pressure taps at the inlet and exit was used to determine the plenum contraction and expansion loss coefficients. The mass flowrate was measured with a laminar flow element, and temperature measurements were taken at the direct inlet and exit of the coupon. Subsequently, the friction factor was calculated.

Bulk convective heat transfer coefficients were measured using a method similar to that outlined by Stimpson et al. [17]. An electrical resistance heater was placed between a copper block and foam insulation, as shown in Fig. 6. The copper block was used in order to exert a constant surface temperature boundary condition on the test coupon. Thermal contact resistance was minimized by applying a thin layer of thermally conductive paste between the coupon and copper blocks. Thermocouples placed in the plenums and foam blocks were used to calculate the conduction losses, which were below 7% of the total input power for all cases.

The convective heat transfer coefficients were determined by calculating the amount heat transferred to the fluid and the log mean temperature difference. The amount of heat transferred to the

fluid resulted from the heat input from the heaters minus any conductive losses. For validation purposes, the outlet temperature measurement was compared to first law analyses and found to agree by equal to or better than 8% for all cases.

Experimental Uncertainty. Measurement uncertainty was determined by the analysis method described by Figliola and Beasley [19]. Pressure drop was the largest contributor to uncertainty for friction factor. The uncertainty for friction factor was below 9% for all Reynolds numbers (Re). The uncertainty in Reynolds number was below 2%. Flow temperature measurements were the largest contributor to Nusselt number uncertainty, which was less than 10% for all cases.

Computational Fluid Dynamics Setup

A conjugate, computational fluid dynamics (CFD) study using a Reynolds Averaged Navier Stokes (RANS) approach was conducted on the same seven coupon geometries to gain further insights into the experimental results. STARCCM+ [20] was used for the conjugate simulations. The turbulence model implemented in these steady RANS simulations was the realizable k - ϵ model. A segregated flow solver was also implemented.

Boundary conditions of the simulations included a velocity inlet of the channel and a pressure outlet at the exit. The pressure outlet for all coupons was set to atmospheric pressure. All CFD simulations were conducted only at $Re = 40,000$. In the heat transfer simulations, uniform heat sources were added to the top surface of the upper copper block and the bottom surface of the lower copper block to match experiments. Identical to the experiments, the copper blocks impose a constant surface temperature on the test coupon. The exposed outer sidewalls of the copper blocks and coupon were set as adiabatic, which was also similar to the experiments having foam blocks on the side. Bulk Nu calculations were made by calculating the log mean temperature difference using the average surface temperature of the wall.

Each of the four components of the coupon model was meshed separately, as shown in Fig. 7. The copper blocks, channel, and fluid domain all used a polyhedral mesher with the fluid domain also using prism layer meshing at the near-wall regions. Meshing the weave pattern, especially with the deep gaps between the tows, proved to be fairly difficult and a few key details were necessary to create a proper mesh. The CAD models of the copper blocks and coupons were imported into STARCCM+ [20] and then the fluid domain was created by conducting a Boolean subtraction from the internal channel of the coupon. When meshing the fluid domain and coupon, increasing the number of cell faces based on the surface curvature was important for capturing the sharp changes in the surface resulting from gaps in the weave tows. Each coupon was between 0.65M and 1.2M cells due to geometry differences. The fluid domain mesh was intentionally varied in order to determine the simulations' degree of grid independence. Nominal mesh sizes for the fluid domain were between 7M and 11M cells. When the mesh size was increased from 10M to 15M cells, Nusselt number calculations varied by a maximum of 2% in one geometry due to the mesh change and by less than 1% in the other six coupons.

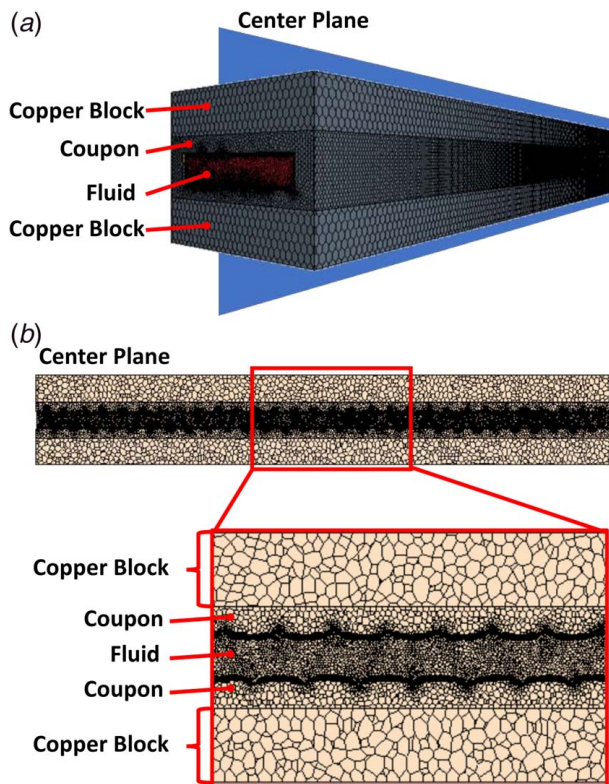


Fig. 7 (a) shows an example of the entire simulation meshes and (b) shows views of the mesh at the center plane of the models

Impact of Hydraulic Diameter Calculation

The friction factor and Nusselt number (Nu) of rectangular channels containing varying orientations and alignments of a 5HS weave surface were measured experimentally and predicted through CFD. Within experimental testing, each coupon geometry was tested between $Re = 5000$ and $50,000$. The experimental tests were benchmarked through the use of a smooth channel coupon in the same rig. The smooth channel data were compared with the Colebrook correlation [21] in Eq. (3) for hydrodynamically smooth ($K_s = 0$) channels through the Reynolds numbers tested.

$$\frac{1}{\sqrt{f_0}} = -2 \log_{10} \left(\frac{K_s}{3.7 D_h} + \frac{2.51}{Re \sqrt{f_0}} \right) \quad (3)$$

For the smooth channel testing, the experimental data agreed with the correlation to within 11% at $Re = 5000$ and to within 5.2% beyond $Re = 7400$ as shown in Fig. 8.

In heat transfer testing, the benchmark data were compared with the Gnielinski correlation [22] as given by Eq. (4) for a hydrodynamically smooth ($K_s/D_h = 0$) pipe through the Reynolds numbers tested.

$$Nu_0 = \frac{\left(\frac{f_0}{8} \right) (Re - 1000) Pr}{1 + 12.7 \left(\frac{f_0}{8} \right)^{0.5} (Pr^{2/3} - 1)} \quad (4)$$

The smooth coupon testing agreed to within 11% of the correlation at $Re = 10,000$ to within 1.5% at $Re = 50,000$ as shown in Fig. 9.

For the coupons containing the weave surface, the friction factors are heavily dependent on the method chosen for calculating each coupon's D_h . By manipulating the Darcy–Weisbach equation, the friction factor can be shown to scale with D_h to the fifth power. This significance can be seen in the friction factor results of Fig. 8. Here, the friction factor of the 0-1W, 0-2W-A, and 0-2W-S coupons using both Methods 1 and 2, previously described, for the D_h calculations are shown along with the smooth channel benchmark. The differences in D_h values cause up to a 62% difference between average friction factor values of a single coupon. As a result of the lower D_h determined through Method 1, friction factors were lower than that of Method 2, even producing values that fall below the Colebrook correlation of a smooth coupon.

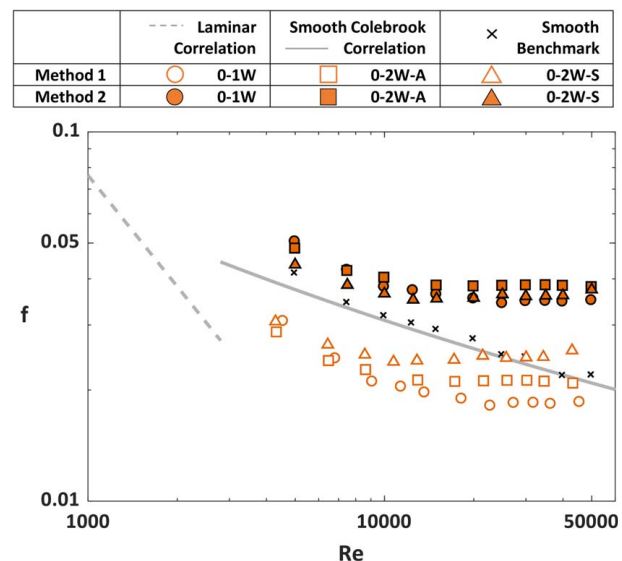


Fig. 8 Friction factor over a range of Reynolds numbers for the 0 deg coupons using D_h calculation methods 1 and 2

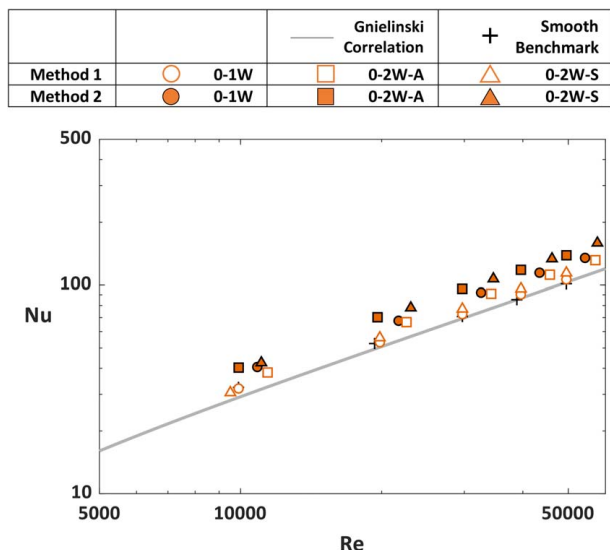


Fig. 9 Nusselt number over a range of Reynolds numbers of the 0 deg coupons using D_h calculation methods 1 and 2

When investigating Methods 1 and 2 for the heat transfer scaling, the resulting Nusselt number values are not as significant as in the friction factor. Figure 9 shows Nusselt numbers using each method for the 0 deg orientation coupons. Similar to the friction factor, Method 2 D_h results in higher Nusselt number values. However, the percent difference between the two methods is only as high as 33%.

These results show the importance of choosing an appropriate scaling dimension such as a hydraulic diameter. In the case of this weave pattern, the wetted surface of the valleys in the weave has a significant influence, which is being captured using Method 1 resulting in D_h values that are low. As will be shown from the CFD predictions, these valleys in the weave surface result in recirculation regions that cause the bulk of the channel flow to travel through the core region. As such, the D_h values that were chosen to be representative of the weave geometry to scale the pressure loss and heat transfer data were calculated with Method 2. All of the data in the following sections used Method 2.

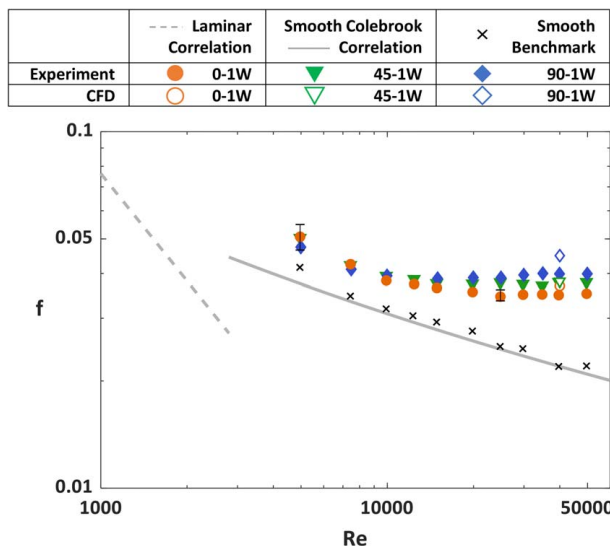


Fig. 10 Friction factor for a range of Reynolds numbers of the coupons containing one weave wall

Weave Orientation Effects for one Wall Coupons

This section reports on the results for coupons containing only one wall with a weave pattern to isolate the effects of weave orientation. This removes additional effects of weave alignment, as seen in the case of two weave walls that will be discussed in the next section. Both friction factor and Nusselt number results, obtained from pressure loss and heat transfer measurements, are reported using Method 2 as described previously for calculating D_h . CFD predictions are also compared and used to further explain the results. The effect of weave orientation for the one wall coupons can be seen in Fig. 10, showing the benchmark measurement along with the experimental and CFD predictions for the three weave orientations evaluated. Maximum and minimum uncertainty bars are shown, with the highest uncertainty occurring at the lowest Re, and uncertainty becoming relatively constant at Re above 25,000. At low Re, there is little difference between the weave orientations; however, as Reynolds number increases beyond $Re > 10,000$ the 90 deg orientation shows the highest friction factor, followed by the 45 deg orientation while the 0 deg orientation has the lowest friction factors. The CFD results show a similar trend at $Re = 40,000$, with the 90 deg orientation having the highest friction factor, but CFD overpredicts the friction factor for all weave orientations.

Augmentation values as a function of Re were also calculated, based on f_0 , defined by Eq. (3), for a smooth channel wall ($K_s = 0$). These augmentation results can be seen in Fig. 11. For $Re < 10,000$, augmentation values are at a minimum of 1.2 for all three weaves but then increased with increasing Re, with the 90 deg orientation showing the highest augmentation. As seen in Fig. 10, the smooth benchmark friction factor decreases with increasing Re, as predicted by the Colebrook correlation, while the friction factors for the coupons having a weaved surface remain constant with increasing Re. These constant friction factors are consistent with behavior seen in rough internal channel flows. The weave acts as surface roughness resulting in a constant friction factor at sufficiently high Re, with the 90 deg orientation having the highest “roughness,” and the 0 deg having the lowest. The CFD predictions at $Re = 40,000$ agree in trends, but both the 90 deg and 0 deg are both overpredicted in terms of augmentation.

Heat transfer results, in terms of Nu, can be seen in Fig. 12, which shows increases in Nu relative to a smooth wall for all weave orientations. Again, the maximum and minimum uncertainty bars are shown, with the highest percent uncertainty occurring at the highest Re, and the lowest percent uncertainty occurring at the lowest Re. The 0 deg and 45 deg orientations have the same heat

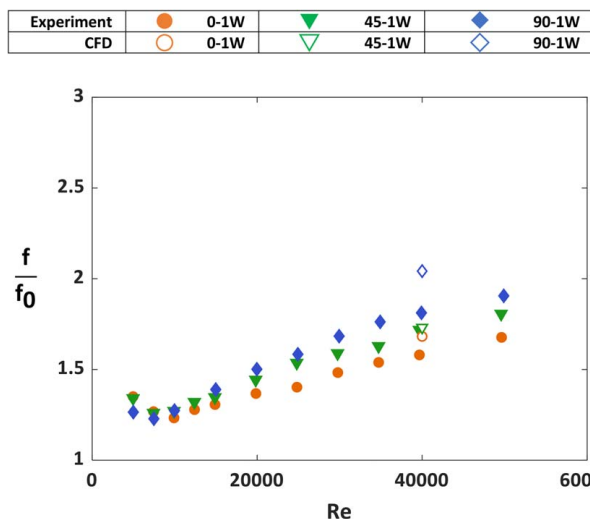


Fig. 11 Friction factor augmentation for a range of Reynolds numbers of the coupons containing one weave wall

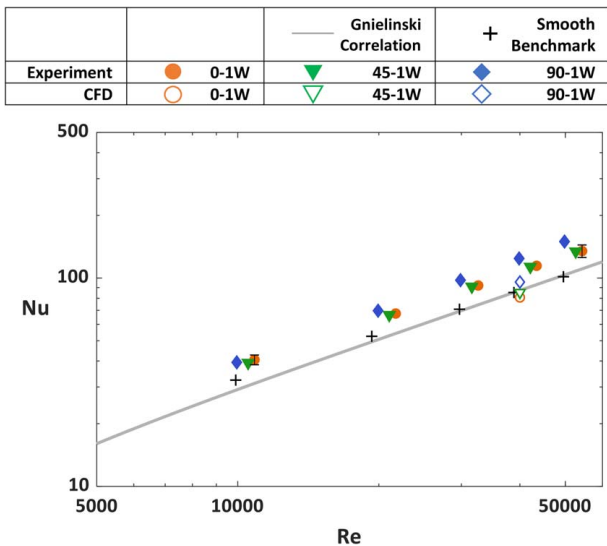


Fig. 12 Nusselt number for a range of Reynolds numbers of the coupons containing one weave wall

transfer performance, while the 90 deg orientation is slightly higher than the other two orientations. The CFD simulations underpredict Nu, but match the same trends seen by the experimental results at $Re = 40,000$.

Heat transfer augmentation values as a function of Re were calculated, based on Nu_0 , defined by Eq. (4), using smooth wall friction factor values from Eq. (3). These augmentation results can be seen in Fig. 13. In contrast to friction factor augmentation levels, the heat transfer augmentations are significantly lower and remain nearly constant with the Reynolds number. This phenomenon of higher friction factor augmentations than heat transfer augmentations is a consistent trend in many different internal channel flows and will be discussed further in a later section. The data in Fig. 13 indicate only a slight increase in augmentations for the 90 deg weave and a slight decrease seen in the 0 deg and 45 deg orientations for increasing Re .

Figure 14 shows predictions of local Nu along the weave wall for the 0 deg, 45 deg, and 90 deg orientations, respectively. Local Nu was calculated using local wall temperatures rather than the average wall temperature used for the bulk Nu calculation. The local wall temperatures of all channels had a maximum standard deviation $3^\circ C$ due to the varying wall thicknesses and flow

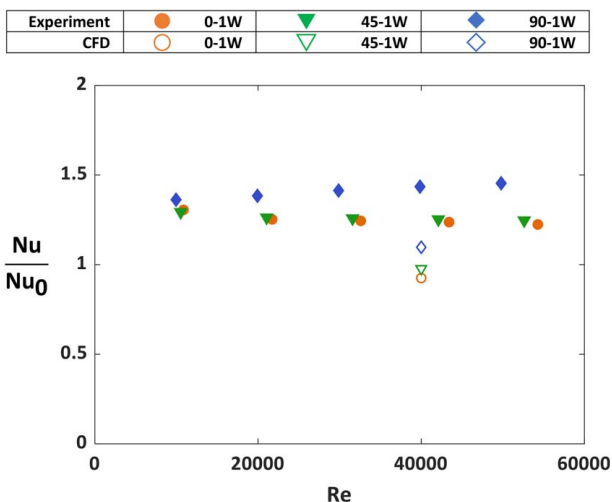


Fig. 13 Nusselt Number augmentation for a range of Reynolds numbers of the coupons containing one weave wall

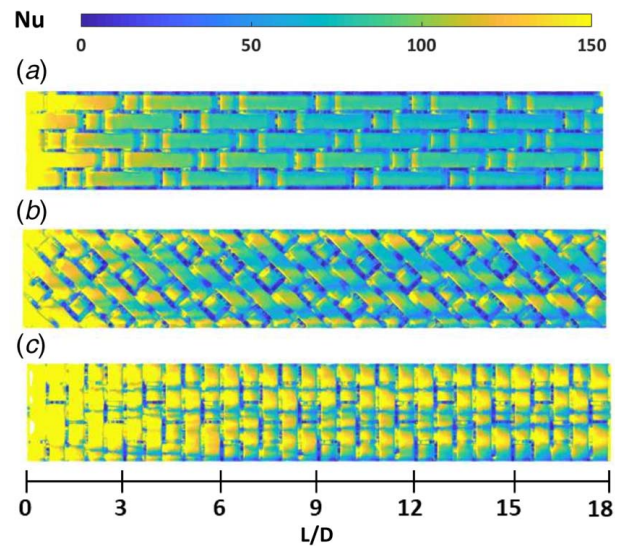


Fig. 14 Top-down view of local Nusselt number contours from CFD for $Re = 40,000$ on the full length of the one weave wall coupons for the (a) 0 deg orientation, (b) 45 deg orientation, and (c) 90 deg orientation

structures caused by the weave geometry. As indicated from the experiments, higher Nusselt numbers result from the 90 deg weave in comparison to the others. For the 0 deg weave, the windward edge of the weave provides a stagnation location for the flow resulting in high heat transfer, which is amplified for the 90 deg case resulting in much higher heat transfer overall as compared to the other weave cases.

Another observation from the Nusselt number contours is that streaks of low Nusselt numbers occur for both the 45 deg and 90 deg cases shown in Figs. 14(b) and 14(c). To better understand the heat transfer phenomena, Fig. 15 shows cross-sectional views of the flow field, with secondary flow vectors and contours of normalized temperature (θ) for the 0 deg, 45 deg, and 90 deg orientations, respectively. For the 0 deg weave in Fig. 15(a), warm fluid remains near the wall with an unmixed core flow and a lack of coherent vortical structures. However, for the 90 deg weave in Fig. 15(c), distinct vortical structures can be seen in the secondary flow vectors that develop into cells of cooler and hotter fluid regions. These differences in secondary flow patterns result in the low and high Nu streaks seen in Fig. 14(c).

Figure 16 shows centerline streamwise views of normalized temperature (θ) within the fully developed region of each channel as well as expanded views of cavity regions for the 0 deg, 45 deg, and 90 deg orientations, respectively. For the 0 deg and 45 deg in Figs. 16(a) and 16(b), stagnant flow recirculation regions can be seen, where the warm fluid remains in the recessed cavities formed by the interlacing cross-sections of the long tow and cross tow weaves. However, in Fig. 16(c) for the 90 deg case, a recirculation region is not apparent with the warm fluid being drawn into the main channel flow. The 90 deg orientation weave has structures that are distinctly different from those seen in the 0 deg orientation and 45 deg orientation, which contributes to an increasing augmentation in Nusselt number with Reynolds number as seen in Fig. 13.

Weave Alignment Effects for Two Wall Coupons

After isolating the one wall effects of the weave, coupons were constructed that included weaves on the two walls having the largest surface areas. In addition, the effect of weave alignment was evaluated. The aligned weave patterns were identical on the top and bottom channel walls, while the staggered weave patterns were offset by $L_{RUC}/2$. These studies were conducted for the 0 deg and 90 deg weave orientations.

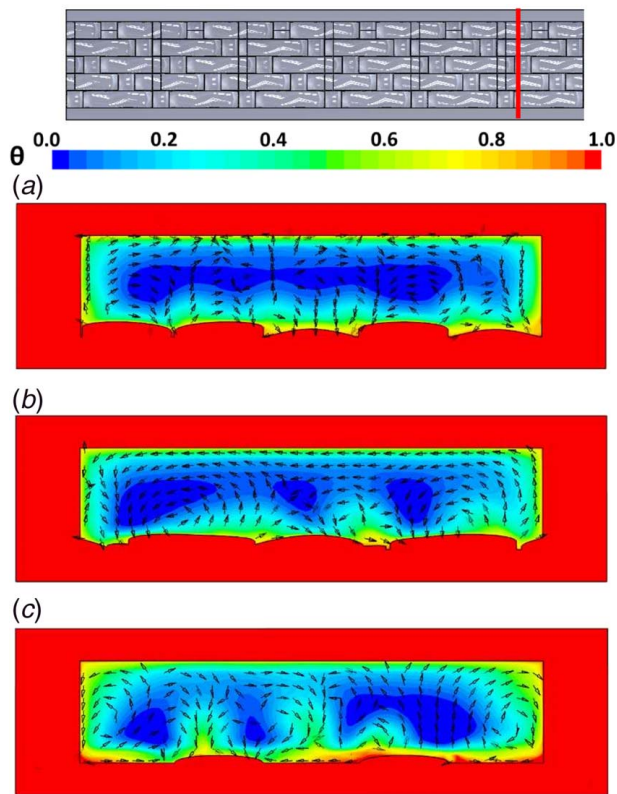


Fig. 15 Cross-sectional view of normalized temperature from CFD at $Re = 40,000$ at an x/L distance of 0.9 for the (a) 0 deg orientation, (b) 45 deg orientation, and (c) 90 deg orientation

Figure 17 shows the measured and predicted friction factor augmentation for all the 0 deg and 90 deg weave coupons including the one wall, two wall aligned, and two wall staggered coupons. The results for the 0 deg weave indicate nearly the same augmentation levels between the one wall and two wall cases. The 90 deg two wall coupons, however, have significantly higher augmentation values as compared with the one wall coupons and have much higher augmentations than the 0° coupons, as expected.

Another noticeable effect in Fig. 17 is for the 90 deg case in terms of whether the weave is aligned or staggered. The aligned case has higher augmentations than the staggered arrangement. In contrast, there is only a small effect for the 0 deg case in terms of whether the weave is aligned or staggered.

As was stated, similar to the one wall results, the augmentation results indicate that the 90 deg orientation angle significantly increased friction factor augmentation for the two wall cases as compared with the 0 deg orientation. This difference was caused by the increased flow separation in the gaps of the 90 deg orientation long tows relative to the lesser separation at cross tow intersections in the 0 deg orientation. Also similar to the one wall coupons, the two wall coupons resulted in increasing friction factor augmentation with Reynolds number because the weaves function similar to rough surfaces in internal channel flow where friction factor is constant with Reynolds number.

As discussed, a clear result in Fig. 17 is that the 90 deg two wall coupons resulted in a large step increase in friction factor augmentation over the 90-1W variant, whereas the 0 deg two wall coupons caused only slight increases over their 0-1W counterpart. This difference is due to the 90-1W coupon having a larger friction factor augmentation than the 0-1W coupon. Therefore, adding a second wall with a 90 deg weave had a more significant impact than adding a second wall with a 0 deg weave. Friction factor augmentation values from the CFD also elaborate on this trend. Although CFD values generally overpredicted the experimental results, adding a second wall with a 90 deg weave caused a more significant

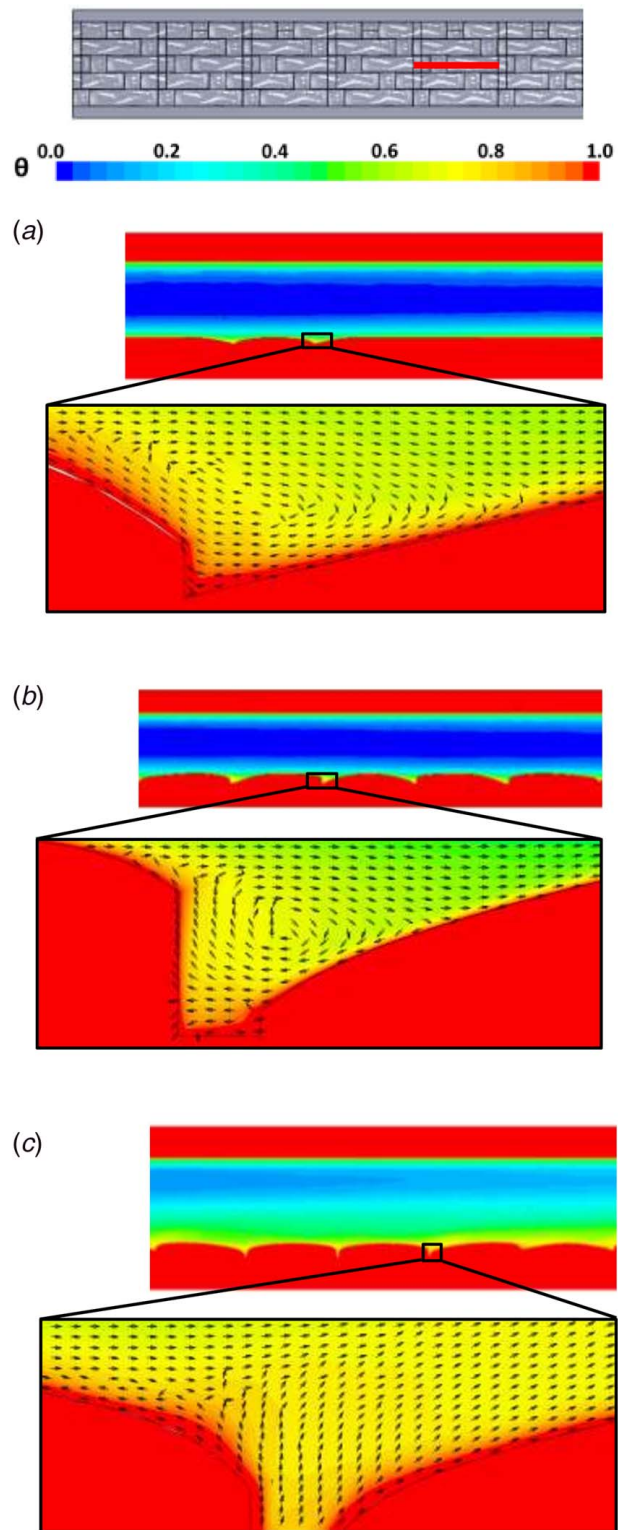


Fig. 16 Normalized temperature fields from CFD at $Re = 40,000$ in the fully developed region of $0.67 < x/L < 0.83$ including expanded views for the (a) 0 deg orientation, (b) 45 deg orientation, and (c) 90 deg orientation

increase in friction factor augmentation compared to the 0 deg. The 90-1W experimental augmentation of 1.9 at $Re = 50,000$ increased to 3.0 and 2.8 for the 90-2W-A and 90-2W-S coupons, respectively. For the 0 deg coupons, the friction factor augmentation increased from 1.7 at $Re = 50,000$ in the 0-1W coupon to 1.8 and 1.8 for the 0-2W-A and 0-2W-S coupons, respectively.

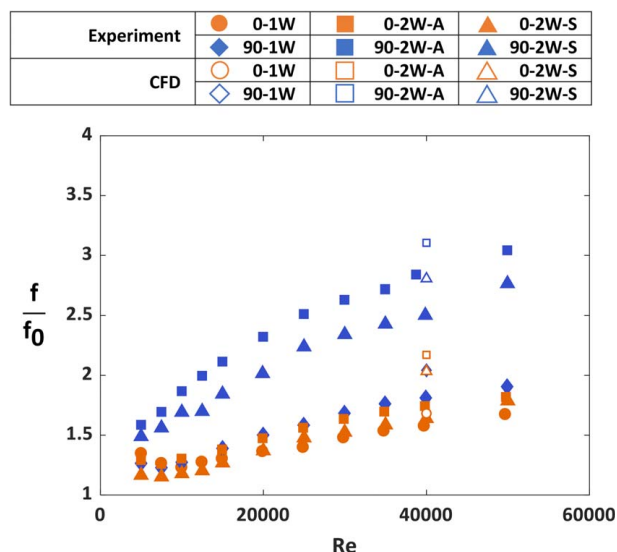


Fig. 17 Friction factor augmentation over a range of Reynolds numbers of the 0 deg and 90 deg coupons containing one and two weave walls

When comparing the two wall coupons in Fig. 17, for both weave orientations in experiments and CFD, the cases where the weave patterns were aligned resulted in larger augmentations than the staggered weaves. Differences in weave alignment can be explained by evaluating the CFD results in Fig. 18, which shows normalized temperature contours with velocity vectors at the centerline entrance regions of the 90-2W-A and 90-2W-S coupons. Near the top and bottom walls of Fig. 18(a), the aligned case indicates accelerated

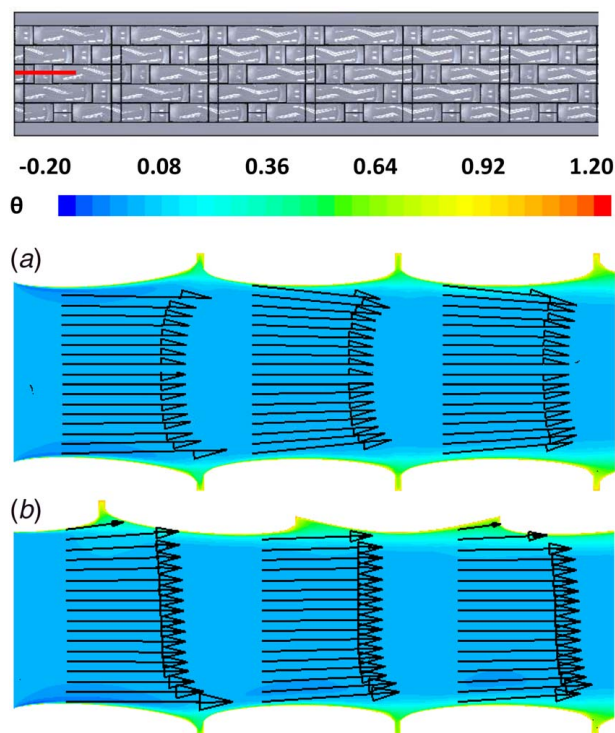


Fig. 18 Normalized temperature contours with velocity vectors at the centerline of the channels between x/L of 0 and 0.1, indicated by the line at the top of the figure, with $Re=40,000$. Figure (a) shows the 90-2W-A coupon and (b) shows the 90-2W-S coupon.

flow near the walls. However, Fig. 18(b) shows an accelerated flow only near the bottom wall due to the staggering. Near-wall velocity differences in the entrance region can be attributed to the initiation of the weave surface. In the aligned case, the weave was initiated at the front of a long tow across the span of the channel. As a result, the flow area contracted resulting in accelerated flow near the wall as it moves across the first tow in the channel. In the staggered case in Fig. 18(b), the bottom wall weave was initiated at the front of a long tow, but the top weave started in the center of a long tow. Consequently, the flow area near the bottom wall contracts, but the flow near the top wall expands as the downstream side of the long tow recedes into the channel wall. The decreased near-wall velocity on the top wall of the staggered cases results in relatively lower shear stress and consequently pressure drop (lower friction factor augmentations) as compared to the aligned cases.

For the measured heat transfer results, the two wall coupons resulted in higher Nusselt number augmentations compared to the one wall coupons, as shown by Fig. 19 for both weave orientations. Overall, the heat transfer augmentations were not as high as the friction factor augmentations, similar to the one wall results. The same trend of Nusselt number augmentation being lower than friction factor augmentation was found in Stimpson et al. [17] for heat transfer within additively manufactured microchannels. The weave roughness, especially in transitions between weave tows where the boundary layer is tripped, significantly affected the friction factor, but did not cause enough mixing in the bulk of the flow to have as large of an effect on Nusselt number.

When comparing Nusselt number augmentations of the aligned and staggered cases in Fig. 19, differences in weave alignment caused very little change in heat transfer. For the 90 deg angle, the aligned case only showed an average augmentation increase of 3% over the staggered while for the 0 deg angle, there was an average percent difference of less than 1% between aligned and staggered cases. This trend is similar to that seen in friction factor augmentation, where the 90 deg aligned and staggered cases showed larger differences than the 0 deg. However, Nusselt number augmentation differences were lower than friction factor augmentation differences between the aligned and staggered coupons.

Insignificant changes in Nusselt number augmentation were also seen in the CFD, where there was less than a 1% difference between the aligned and staggered cases for both weave orientations. Although much more subtle than the friction factor, the slight

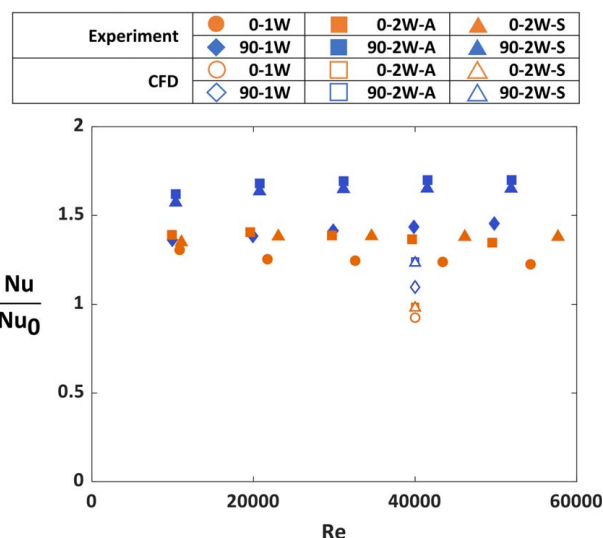


Fig. 19 Nusselt number augmentation over a range of Reynolds numbers of the 0 deg and 90 deg coupons containing one and two weave walls

differences in Nusselt number augmentation for the 90 deg two wall coupons are explained by the same flow contractions and expansions caused by differing initiations in the weave patterns. The decrease in Nusselt number augmentation of the 90-2W-S coupon is caused by the decrease in flow velocity near the top wall, as shown in Fig. 18(b). The temperature contours of Fig. 18 show decreased fluid temperatures near the walls where the flow accelerated, thereby increasing the fluid and surface temperature difference in those areas and increasing the amount of local convective heat transfer. On the top wall of Fig. 18(b), the flow had lower velocity than the bottom wall and did not decrease in temperature, comparatively reducing the local Nusselt number.

The pressure drop and heat transfer results of this study were also compared to additively manufactured microchannels from Stimpson et al. [17] and parallel rib channels from Park et al. [23]. The ribbed channels were composed of two ribbed walls along the width and smooth walls along the shorter side walls. All of the ribs were spaced by $p/e = 10$. The AR of the coupons being compared were 5 for the 5HS weave channels, 2 and 4 for the ribbed channels, and 2.3 and 2.1 for the microchannels. Figure 20 shows friction factor augmentation versus Nusselt number augmentation of the scaled-up 5HS weave geometries, rib channels, and additive microchannels. The data taken for the rectangular microchannels are shown for a similar Reynolds number range up to $Re = 20,000$ [17], while the rib channels were from 10,000 to 60,000 [23].

In Fig. 20, the 5HS weave, the 90 deg two wall channels attained the highest Nusselt number augmentation and also the highest friction factor augmentation for the weave coupons. In fact, the relatively small increase in Nusselt number augmentation from the 90 deg two wall coupons cost a large increase in friction factor augmentation.

The friction factor augmentation difference in the rib angles was much larger than the differences seen in the 5HS weave as shown in

5HS Weave, AR = 5	○ 0-1W	■ 0-2W-A	▲ 0-2W-S
	▼ 45-1W	■ 90-2W-A	▲ 90-2W-S
Stimpson et al. [17]	◆ 90-1W	+	×
		Rectangle, AR = 2.3	Rectangle, AR = 2.1
Park et al. [23]	AR = 2 $e/D_h = 0.047$ $p/e = 10$	★ 45°-Rib	★ 90°-Rib
	AR = 4 $e/D_h = 0.078$ $p/e = 10$	◀ 45°-Rib	▶ 90°-Rib

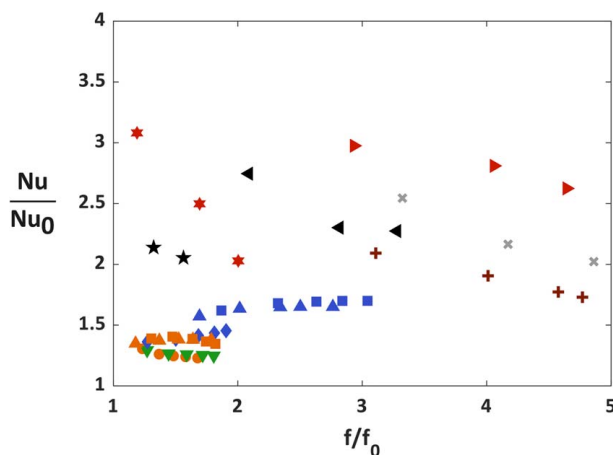


Fig. 20 Nusselt number and friction factor augmentations of all weave geometries compared to additively manufactured microchannels from Stimpson et al. [17] and ribbed channels from Park et al. [23]. Aspect ratios of the weave channels are all 5. Aspect ratios of the ribbed channels are 2 and 4. Aspect ratios 2.3 and 2.1 of the microchannels are named L-1x-In and M-2x-In, respectively, in Stimpson et al. [17].

Fig. 20. Note the 45 deg rib was able to achieve the same Nusselt number augmentation as the 90 deg rib at low friction factor augmentation before dropping below the 90 deg rib at $AR = 4$. With the 5HS weave, the same trend was present. When comparing to the rectangular microchannels with additive roughness [17], the weave channels generally exhibited lower Nusselt number augmentation and much lower friction factor augmentation.

The same comparisons between different internal channels were also made using a thermal performance parameter (TPP), Eq. (5), which is used to evaluate the benefits of increased heat transfer against the detriment of increased pressure drop.

$$TPP = \frac{Nu/Nu_0}{(f/f_0)^{1/3}} \quad (5)$$

Figure 21 shows comparisons of TPP versus Reynolds number for the same internal channels seen in Fig. 20, the 5 HS weave channel geometries, rib channels, and additive microchannels. The data were taken at a range $Re = 5000$ – $60,000$.

In Fig. 21, the 0-2W-A coupon performed slightly better than the rest, with the 0 deg two wall and 90 deg coupons performing similarly throughout the range of Reynolds numbers. Especially at high Reynolds numbers, the 0-1W and 45-1W coupons saw lower TPP than the other coupons. Additionally, all coupons saw decreases in TPP with increases in Reynolds number.

For the rib channels, the $AR = 2$ channels saw increases in TPP throughout the range of Reynolds numbers. Additionally, the $AR = 2$ rib channels were more sensitive to rib angle compared to the $AR = 4$, but all channels also saw decreases in TPP with increasing Reynolds number. This same trend is seen in the additively manufactured microchannels, but these channels show lower TPP compared to both the rib channels and 5HS channels when compared at the same Reynolds number. As a result of these comparisons, the weave pattern is shown to exhibit unique pressure drop and heat transfer performance relative to other types of internal roughness.

5HS Weave, AR = 5	○ 0-1W	■ 0-2W-A	▲ 0-2W-S
	▼ 45-1W	■ 90-2W-A	▲ 90-2W-S
Stimpson et al. [17]	◆ 90-1W	+	×
		Rectangle, AR = 2.3	Rectangle, AR = 2.1
Park et al. [23]	AR = 2 $e/D_h = 0.047$ $p/e = 10$	★ 45°-Rib	★ 90°-Rib
	AR = 4 $e/D_h = 0.078$ $p/e = 10$	◀ 45°-Rib	▶ 90°-Rib

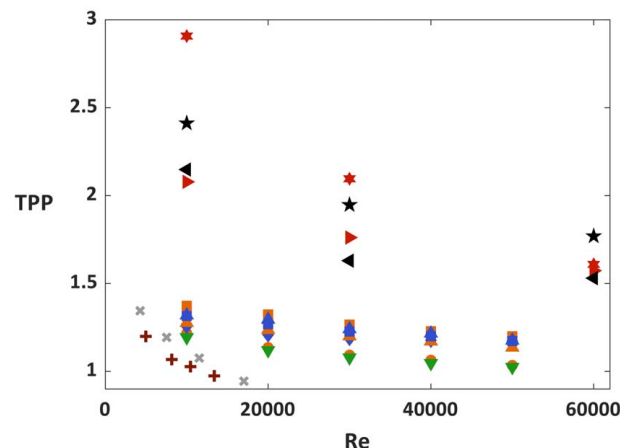


Fig. 21 Thermal performance parameter versus Reynolds number for weave geometries, microchannels from Stimpson et al. [17] and ribbed channels from Park et al. [23]

Conclusion

Experimental and computational studies assessed the effects of a woven surface pattern, representative of a CMC surface, on pressure loss and convective heat transfer performance within an internal channel. Experimental coupons were additively manufactured with differing orientations of a 5 HS weave pattern overlaid onto the walls of rectangular channels. Pressure drop and heat transfer were measured through the channels over a range of Reynolds numbers from 5000 to 50,000. CFD predictions were made on the same channels at $Re = 40,000$ for further understanding of the weave surface effects.

The friction factor and Nusselt number scaling highlighted the significance of appropriate hydraulic diameter for the complex weave geometry. In using a method that fully accounted for the valleys of weave, an artificially high wetted perimeter resulted due to the valley weaves. The data indicated that it was most suitable to use a rectangular channel that was fit to the average wall heights of the weave.

In the 0 deg orientation, the long tows of the 5HS weave resulted in lower friction factor and Nusselt numbers than in the 90 deg weave orientation where the long tows were perpendicular to the flow direction. Flow fields predicted through CFD showed flow separations within the valleys of the weave resulting in large pressure losses.

Heat transfer coefficients were also measured to be higher in the case of the 90° weave relative to the 0 deg weave; however, augmentations were much lower than the friction factor augmentations. The flow fields indicated that the nearly stagnant flow regions within the valleys of the weave led to poor flow mixing. In general, increases in local Nusselt number occurred on the upstream sides of weave tows, while decreases occurred at the flow separation regions on the downstream sides of weave tows and in the gaps between weave tows. Local Nusselt number contours showed streaky patterns for the 45 deg and 90 deg weave orientations resulting from secondary flow patterns in the channel. However, only the 90 deg orientation showed distinct secondary flow vortical structures that caused mixing between the main flow and the stagnant fluid regions.

The effects of two weave wall channels along with weave alignment were evaluated for the 0 deg and 90 deg orientations. For both orientations, adding a second weave surface increased friction factor and Nusselt number augmentations. These increases were more significant for the 90 deg weave because of the increased flow separation and turbulent mixing associated with that orientation. Measurements indicated higher friction factor augmentations in the channels with the surface weave patterns aligned as opposed to staggered. CFD simulations showed that the differences in augmentation were most influenced by the initiation of the weave pattern at the channel inlet, which was identified as the reason for the higher values for the aligned case. Nusselt number augmentation was not significantly affected by the initiation of the weave, with results showing little difference between the aligned and staggered weaves.

Overall pressure loss and heat transfer performance of the weave surfaces were compared to additively manufactured microchannels and rectangular channels with parallel ribs. The weave channels exhibited lower Nusselt number augmentation than the rib channels as well as the additively manufactured microchannels. Similar to the ribbed channels, the weave channels showed increased augmentation values in the 90 deg orientation compared to the 45 deg. In terms of TPP, the 0-2W-A had the highest performance, but all 0 deg two wall and 90 deg coupons performed similarly, with the 0-1W and 45-1W having lower performance values across all Reynolds numbers.

Results of this study contribute to the knowledge of weave surface topology, representative of CMC surfaces, on pressure drop and heat transfer within internal channel flow. This knowledge can help predict the internal cooling performance of turbine components with relevant surface patterns such as those made of CMCs.

These results can also be used by the designer to orient the weave pattern in a favorable direction within the component.

Acknowledgment

The authors would like to thank Pratt & Whitney for their technical and financial support of the research for this paper. Computations for this research were performed on the Pennsylvania State University's Institute for Computational and Data Sciences' Roar supercomputer.

Conflict of Interest

There are no conflicts of interest.

Data Availability Statement

The authors attest that all data for this study are included in the paper.

Nomenclature

e	= rib height
f	= friction factor, $2D_h/L \Delta P/\rho v^2$
h	= convective heat transfer coefficient, $Q_{flow}/A_s \Delta T_{LM}$
p	= rib spacing
u	= mass-averaged velocity
H	= channel height
W	= channel width
M	= number of surface data points
N	= number of slices
P	= channel perimeter
T	= flow temperature
h_f	= fabric height
h_w	= weave peak
w_t	= tow width
s_t	= tow pitch
z_{des}	= design intent RUC surface height
z_{surf}	= actual RUC surface height
A_c	= channel cross-sectional area
D_h	= hydraulic diameter
K_s	= sandgrain roughness
T_{in}	= inlet flow temperature
T_s	= channel surface temperature
AR	= channel aspect ratio
Re	= Reynolds number, uD_h/ν
Nu	= Nusselt number, hD_h/k
Pr	= Prandtl number
RMS _w	= root mean square roughness of the weave
RUC	= repeating unit cell
TPP	= thermal performance parameter

Greek Symbols

θ	= normalized temperature, $T - T_{in}/T_s - T_{in}$
ν	= kinematic viscosity
ρ	= fluid density

Subscript

0 = reference condition

References

- [1] Yin, X. W., Cheng, L. F., Zhang, L. T., Travitzky, N., and Greil, P., 2017, "Fibre-Reinforced Multifunctional SiC Matrix Composite Materials," *Int. Mater. Rev.*, **62**(3), pp. 117–172.
- [2] Chawla, K. K., 1998, "Chapter 7: Ceramic Matrix Composites," *Composite Materials*, Springer, Berlin, pp. 212–251.

- [3] Ohnabe, H., Masaki, S., Onozuka, M., Miyahara, K., and Sasa, T., 1999, "Potential Application of Ceramic Matrix Composites to Aero-Engine Components," *Compos. Part A Appl. Sci. Manuf.*, **30**(4), pp. 489–496.
- [4] Walock, M. J., Heng, V., Nieto, A., Ghoshal, A., Murugan, M., and Driemeyer, D., 2018, "Ceramic Matrix Composite Materials for Engine Exhaust Systems on Next-Generation Vertical Lift Vehicles," *ASME J. Eng. Gas Turbines Power*, **140**(10), p. 102101.
- [5] Tong, M. T., 2010, "An Assessment of the Impact of Emerging High-Temperature Materials on Engine Cycle Performance," GT2010-22361.
- [6] Zhu, D., 2018, "Aerospace Ceramic Materials: Thermal, Environmental Barrier Coatings and SiC/SiC Ceramic Matrix Composites for Turbine Engine Applications," NASA/TM 2018-219884.
- [7] Alvin, M. A., Anderson, I., Heidloff, A., White, E., Bhatt, R., Grady, J., McMordie, B., and Warnes, B., 2015, "Development of Advanced Material Systems for Future Gas Turbine Applications," Turbo Expo: Power for Land, Sea, and Air, GT2015-43456.
- [8] Presby, M. J., Nesredin, K., Sanchez, L. J., Faucett, D. C., Choi, S. R., and Morscher, G. N., 2019, "Life-Limiting Behavior of an Oxide/Oxide Ceramic Matrix Composite at Elevated Temperature Subject to Foreign Object Damage," *ASME J. Eng. Gas Turbines Power*, **141**(3), p. 031012.
- [9] Dassios, K. G., Aggelis, D. G., Kordatos, E. Z., and Matikas, T. E., 2013, "Cyclic Loading of a SiC-Fiber Reinforced Ceramic Matrix Composite Reveals Damage Mechanisms and Thermal Residual Stress State," *Compos. Part A Appl. Sci. Manuf.*, **44**(1), pp. 105–113.
- [10] Watanabe, F., Nakamura, T., and Mizokami, Y., 2017, "Design and Testing for Ceramic Matrix Composite Turbine Vane," GT2017-63264.
- [11] Watanabe, F., Nakamura, T., and Shinohara, K. I., 2016, "The Application of Ceramic Matrix Composite to Low Pressure Turbine Blade," GT2016-56614.
- [12] Krishna, K., Ricklick, M., Poinssatte, P., and Thurman, D., 2016, "Preliminary Investigation of an Oblique Jet Impingement Cooling on CMC Rough Surface," 52nd AIAA/SAE/ASEE Joint Propulsion Conference, AIAA 2016-4851.
- [13] Krishna, K., and Ricklick, M., 2017, "Heat Transfer Analysis of Jet Impingement Cooling on a Simulated Ceramic Matrix Composite Surface," GT2017-64991.
- [14] Wilkins, P. H., Lynch, S. P., Thole, K. A., Quach, S., and Vincent, T., 2020, "Experimental Heat Transfer and Boundary Layer Measurements on a Ceramic Matrix Composite Surface," GT2020-15053.
- [15] Nemeth, N. N., Mital, S. K., and Lang, J., 2010, "Evaluation of Solid Modeling Software for Finite Element Analysis of Woven Ceramic Matrix Composites," NASA/TM 2010-216250.
- [16] TEXGEN, 2007, Version 3.11.0, User's Guide.
- [17] Stimpson, C. K., Snyder, J. C., Thole, K. A., and Mongillo, D., 2016, "Roughness Effects on Flow and Heat Transfer for Additively Manufactured Channels," *ASME J. Turbomach.*, **138**(5), p. 051008.
- [18] Snyder, J. C., Stimpson, C. K., Thole, K. A., and Mongillo, D., 2016, "Build Direction Effects on Additively Manufactured Channels," *ASME J. Turbomach.*, **138**(5), p. 051006.
- [19] Figliola, R. S., and Beasley, D. E., 1995, "Theory and Design for Mechanical Measurements, 2nd ed.," Eur. J. Eng. Educ., **20**(3), pp. 386–387.
- [20] STARCCM+, Version 14.04.011, Product Overview.
- [21] Colebrook, C. F., Blench, T., Chatley, H., Essex, E. H., Finnicome, J. R., Lacey, G., Williamson, J., and Macdonald, G. G., 1939, "Correspondence. Turbulent Flow in Pipes, With Particular Reference to the Transition Region Between the Smooth and Rough Pipe Laws," *J. Inst. Civ. Eng.*, **12**(8), pp. 393–422.
- [22] Gnielinski, V., 1976, "New Equations for Heat and Mass Transfer in Turbulent Pipe and Channel Flow," *Int. Chem. Eng.*, **16**(2), pp. 359–368.
- [23] Park, J. S., Han, J. C., Huang, Y., Ou, S., and Boyle, R. J., 1992, "Heat Transfer Performance Comparisons of Five Different Rectangular Channels with Parallel Angled Ribs," *Int. J. Heat Mass Transfer*, **35**(11), pp. 2891–2903.